Strain-explorable valley-polarized topological phase transition and perpendicular magnetocrystalline anisotropy in hexagonal *M*ClBr (*M* = Ru, Os) monolayers

Zeyu Zhang,[1,*] He Huang,[1,*,†] Liming Wang,[2] Yanzhe Zhao,[1] Chuang Liu,[1] Shiming Zhou,[2] Yanfei Wu,[1] Jiapeng Zhao,[1] Guanxiong Qiao,[1] Dingsong Wang,[1] Jingyan Zhang,[1] Xinqi Zheng,[1] and Shouguo Wang[1,2,‡]

[1]*School of Materials Science and Engineering, Beijing Advanced Innovation Center for Materials Genome Engineering, University of Science and Technology Beijing, Beijing 100083, China*

[2]*Anhui Key Laboratory of Magnetic Functional Materials and Devices, School of Materials Science and Engineering, Anhui University, Hefei 230601, China*

(Received 5 February 2024; revised 28 April 2024; accepted 17 June 2024; published 10 July 2024)

The coexistence of ferrovalley and band topology has garnered significant attention, due to its valley-polarized quantum anomalous Hall effect in condensed matter physics for two-dimensional (2D) ferromagnetic materials, in which the spontaneous out-of-plane magnetization and strong spin-orbit coupling effect are both satisfied. Here, using first-principles calculations and a tight-binding model, we reported the valley-polarized band topological phase transition and perpendicular magnetocrystalline anisotropy in a series of 2D Janus magnetic transition metal dihalides *H*-*M*ClBr (*M* = Ru, Os) via strain manipulation. Due to both the inversion and time-reversal asymmetry, valley polarization could be spontaneously achieved in hexagonal RuClBr and hexagonal OsClBr monolayers, with considerable values of 247 and 150 meV, respectively, which exceed those of most reported 2D ferrovalley materials. By applying an external biaxial strain, it is noteworthy that the easy magnetization axis of *H*-RuClBr can be switched to the out-of-plane direction due to distinct spin channel interactions between the Ru *d* orbitals. Moreover, transitions from the anomalous valley Hall effect to the nontrivial topological state in both *H*-RuClBr and *H*-OsClBr are observed. Due to the spontaneous valley polarization, band topology phase transition, and perpendicular magnetocrystalline anisotropy, it is expected that 2D Janus magnetic transition metal dihalides expand the application for the interplay among valleytronics, spintronics, and band topology.

DOI: 10.1103/PhysRevB.110.035128

I. INTRODUCTION

The valley, as the local minimum or maximum of a band structure in momentum space [1–3], offers a valley degree of freedom for information technology analogous to charge and spin in spintronics. This degree of freedom is known in the field of valleytronics and is robust against scatterings of smooth phonons and deformations [4–6], benefiting from its degeneracy-induced unequal K and $-K$ valley separation in the Brillouin zone (BZ). The opposite Berry curvature appears in two valleys and electrons gain transverse velocities in the presence of an external electric field, giving rise to the anomalous valley Hall effect (AVHE). In previous research, two-dimensional (2D) transition metal disulfides (TMDs) have attracted great attention based on valley-dependent optical selection rules. For example, circularly polarized optical pumping can generate valley polarization in MoS_2 [7] and $MoSe_2$ [8]. Unfortunately, the valleys in these 2D TMDs are subject to an inherently short carrier lifetime, leading to information loss when optical pumping is withdrawn. More attempts have been made, such as applying magnetic doping [9–13], magnetic field, and magnetic proximity effect [14,15]. However, these external methods lead to phonon scattering and integration complexity of host materials.

Similar to 2D ferromagnetic (FM) materials, 2D ferrovalley (FV) materials with intrinsic magnetism and time-reversal asymmetry can produce spontaneous valley polarization and corresponding AVHE. Until now, several 2D FV materials have been studied, such as *H*-VS_2, VSi_2N_4, VSi_2P_4, Nb_3I_8, $VAgP_2Se_6$, and $TiBr_2$ [9,12,16–18], but the majority of them are not suitable for practical valleytronics due to either low Curie temperatures (T_C) or in-plane easy magnetization axis, requiring difficult manipulation of the easy magnetization axis switching to the out-of-plane direction for spontaneous valley polarization. Although several FV materials are found with out-of-plane magnetization, such as *H*-$FeCl_2$ and VSi_2P_4, the limited valley polarization values impede the observation of AVHE and restrict their applications in actual valleytronic devices. Therefore, the search for 2D FV materials with spontaneous considerable valley polarization and out-of-plane magnetization becomes the main challenge. Recently, MX_2 (M = Ru, Os; X = I, Cl, Br) FV materials with high T_C and large valley polarization have attracted considerable attention [18–21]. Specifically, $RuCl_2$ and $OsBr_2$ exhibit remarkable T_C of up to 260 and 350 K, respectively [19,21], while $OsBr_2$ demonstrates an impressive valley polarization value of up to 530 K [18].

*These authors contributed equally to this work.
†Contact author: hhuang@ustb.edu.cn
‡Contact author: sgwang@ustb.edu.cn

Meanwhile, the combination of ferrovalley index and topology into one single material system gives rise to the valley-polarized quantum anomalous Hall effect (VQAHE) and half-valley-metal (HVM) phase in condensed matter physics and materials science, which is likely to yield novel physics and emerging applications. Recently, several studies have witnessed ferrovalley-based topological phase transitions via correlation effect and external stimuli such as strain engineering, as observed in $VSiGeP_2As_2$, *H*-$FeCl_2$, *H*-ScI_2, *H*-(Ru, Os)Br_2, and VSi_2P_4 [16–18,22–25] monolayers. Compared to *H*-MX_2, the Janus variant of the MXX' phase with two different chalcogen layers has spontaneous mirror symmetry breaking. The out-of-plane asymmetry between the X and X' layers can significantly affect the magnetic exchange effect and multiferroic properties. Furthermore, stable Janus group VI chalcogenides MXY (M = Mo, W; X, Y = S, Se, Te; $X \neq Y$) were first proposed by Cheng *et al.* [26], and the Janus MoSSe was successfully synthesized via modified chemical vapor deposition (CVD) methods [27]. The MXY (M = Y, Ru, Os; X, Y = Br, Cl, F, I) material is an excellent two-dimensional Janus material due to its significant valley polarization values and the emergence of topological states with varying Hubbard U values [28–32]. Consequently, gaining more insights into the intrinsic topologically nontrivial ferrovalley behavior of these 2D Janus materials is necessary.

In this work, by using first-principles calculations and a tight-binding model, we reported the valley-polarized band topological phase transition and perpendicular magnetocrystalline anisotropy in a series of Janus magnetic transition metal dihalides *H*-*M*ClBr (M = Ru, Os) monolayers via strain manipulation. Owing to both the inversion asymmetry and time-reversal asymmetry, spontaneous valley polarization could be realized in *H*-RuClBr and *H*-OsClBr with values of 247 and 150 meV, respectively, which are beneficial for the experimental AVHE observation. Moreover, *H*-OsClBr favors a pristine out-of-plane magnetization with a large magnetic anisotropy energy (MAE) value of 11.89 meV per unit cell, while the second-order perturbation analysis of MAE demonstrates that the easy magnetization axis of *H*-RuClBr can be switched from the in-plane to the out-of-plane direction via a compressive strain. More interestingly, the transition from anomalous valley Hall effect to nontrivial topological state in both *H*-RuClBr and *H*-OsClBr is also observed under biaxial strain, which can expand the novel applications for the interplay among valleytronics, spintronics, and band topology.

II. COMPUTATIONAL METHODS

All calculations in this work were performed in the Vienna *Ab initio* Simulation Package (VASP) based on density functional theory (DFT) [33–36]. The generalized gradient approximation (GGA) of the Perdew-Burke-Ernzerhof (PBE) functional was used to treat the electron exchange-related interactions. A vacuum space of 30 Å was adopted in the nonperiodic z direction to avoid interactions between adjacent images. To account for the robust exchange of localized d electrons, an effective on-site Hubbard PBE+U method was utilized with the U_{eff} values of 2.5 and 1.8 eV for Ru 4d and Os 5d orbitals [18], respectively. The kinetic energy cutoff for the plane-wave basis was set to 520 eV. All structures were fully relaxed until the total energy and force convergency acting on each atom were below 10^{-5} eV and 0.02 eV/Å. The Brillouin zone integration was sampled with a Γ-centered $13 \times 13 \times 1$ k mesh for each unit cell.

The phonon dispersions of *H*-RuClBr and *H*-OsClBr were obtained using a frozen phonon method with the assistance of PHONOPY code. A $4 \times 4 \times 1$ supercell with a Γ-centered $3 \times 3 \times 1$ k-point grid was adopted for phonon calculations [37]. To check the thermodynamic stability, *ab initio* molecular dynamics (AIMD) simulations were performed at temperatures of 300 and 150 K by using the *N*-*V*-*T* ensemble with the Nosé-Hoover thermal bath method for *H*-RuClBr and *H*-OsClBr, respectively. A $4 \times 4 \times 1$ supercell was considered and the AIMD simulation lasted 10 ps with a time step of 2.0 fs. To determine the magnetic ground state of *H*-RuClBr and *H*-OsClBr, we compare the total energies using a $2 \times 2 \times 1$ supercell for the FM and antiferromagnetic (AFM) configurations. The Metropolis Monte Carlo (MC) calculation was conducted to simulate the magnetic phase transition Curie temperature by using the VAMPIRE package [38]. A $100 \times 100 \times 1$ supercell was adopted for each monolayer during the MC simulations. The spin flips randomly 10^7 MC simulation steps at each temperature. The spin-resolved and orbit-resolved band structures were abstracted by using the VASPKIT software [39]. The Berry curvature and anomalous Hall conductivity were realized by constructing maximally localized Wannier functions (MLWFs) [40] using the WANNIER90 package. To obtain the topological band-edge state, a tight-binding Hamiltonian with the basis of MLWFs was calculated by using the Wannier Tools package [41]. The data of the MAE distribution in the Brillouin region were extracted from energy bands $E_n(k)$ displaying d_i orbital character in the OUTCAR and PROCAR file generated by the MAE calculation using VASP.

III. RESULTS AND DISCUSSION

A. Structure and stability

The top and side views of the single-layer *H*-*M*ClBr (M = Ru, Os) lattice are shown in Fig. 1(a). In analogy to other TMDs, the *H*-*M*ClBr monolayer belongs to the $P\bar{3}m1$ space group. The Ru/Os atomic layer is sandwiched by up Cl and down Br atomic layers, respectively, thus forming a Janus trigonal prismatic structure and intrinsic inversion symmetry breaking. Each unit cell of *H*-*M*ClBr possesses one M, one Cl, and one Br atom. The optimal lattice parameters of *H*-RuClBr and *H*-OsClBr are 3.66 and 3.56 Å, respectively, which are consistent with previous work [31]. Figure 1(b) illustrates the electron localization function (ELF) of *H*-RuClBr, where one can see that electrons are mainly located around Cl and Br atoms, indicating the ionic bonding characteristics of *M*-Cl and *M*-Br bonds. The valence electron configuration of the Ru/Os atom is $4d^7 5s^1/5d^6 4s^2$. After donating two electrons to neighboring Cl and Br atoms, Ru^{2+} and Os^{2+} ions are left with only six valence electrons. In the presence of a trigonal prismatic crystal field, as shown in Fig. 1(b), the d orbitals of the Ru and Os atoms undergo a splitting into three distinct groups: one a orbital (d_{z^2}), two e_1 orbitals (d_{xy} and $d_{x^2-y^2}$),

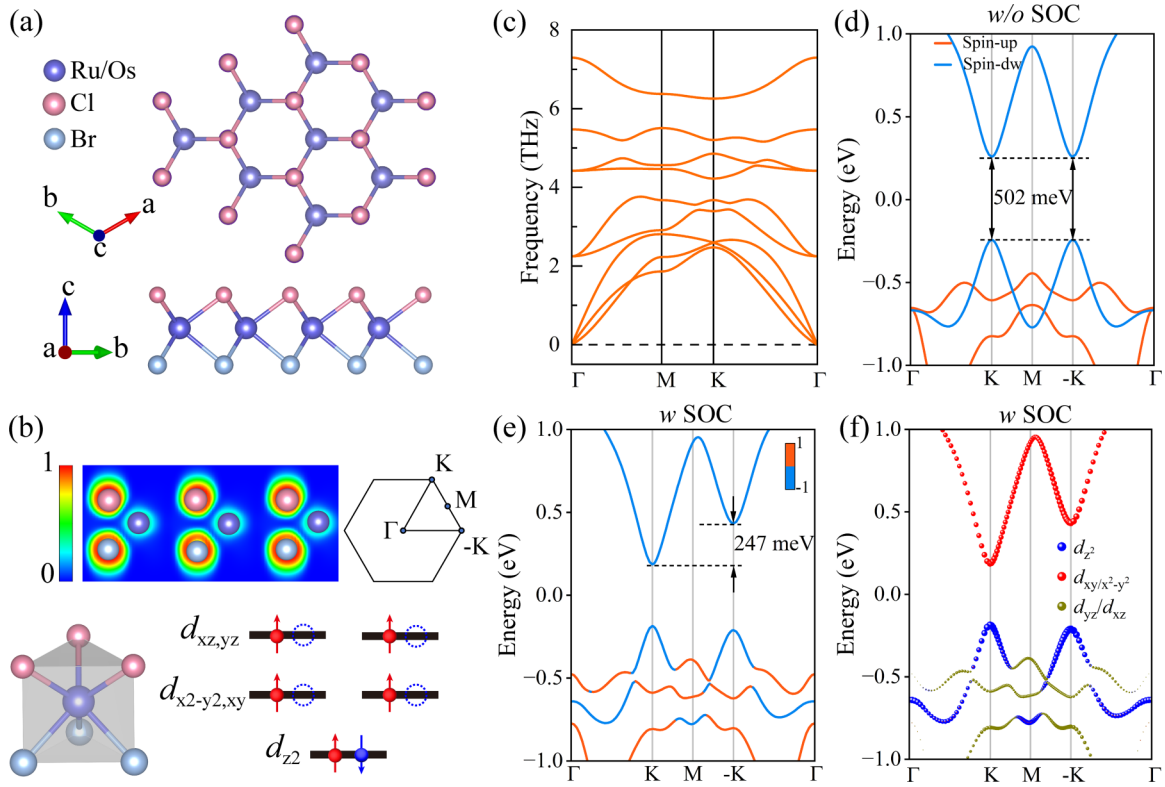

FIG. 1. (a) Crystal structure of *H*-*M*ClBr (M = Ru, Os) from the top and side views. (b) Electron localization function of *H*-RuClBr, 2D Brillouin zone with high-symmetry points, and the splitting of d orbitals under the trigonal prismatic crystal field. (c) Phonon spectra of *H*-RuClBr. [(d) and (e)] Spin-polarized band structures of *H*-RuClBr without and with SOC. Red and blue represent the spin-up and spin-down states, respectively. (f) Orbital-resolved band structures of *H*-RuClBr with SOC.

and two e_2 orbitals (d_{yz} and d_{xz}). As illustrated in Fig. 6(d) and Fig. S1(b) in the Supplemental Material [42], the spin-up electrons occupy all the d orbitals, while the spin-down electrons only occupy the d_{z^2} orbital. Therefore, the valence electron configurations of Ru^{2+} and Os^{2+} ions are both $a^2e_1^1e_2^1$ with the theoretical magnetic moment of 4 μ_B. The calculation results show that the magnetic moments of *H*-RuClBr and *H*-OsClBr are 3.724 μ_B and 4.016 μ_B, respectively, which are very close to the formal atomic magnetic moment of 4 μ_B. The phonon spectra depicted in Fig. 1(c) and Fig. S1(a) confirm the dynamic stabilities of *H*-RuClBr and *H*-OsClBr, as there are no imaginary frequencies present. To verify the thermodynamic stabilities of *H*-RuClBr and *H*-OsClBr, a 4 × 4 × 1 supercell is adopted in the AIMD calculations at 300 and 150 K with a time duration of 10 ps. The total energies of *H*-RuClBr and *H*-OsClBr, as revealed in Fig. S2 [42], exhibit stability around their equilibrium values. Additionally, it is worth noting that no structural rearrangements are observed in the structural snapshots, thereby indicating the thermodynamic stabilities of *H*-RuClBr and *H*-OsClBr at finite temperatures. Currently, the preparation technology for different phases of TMDs has reached a relatively advanced stage. For instance, *H*-MoS_2 can be directly synthesized using metal-organic chemical vapor deposition [43], *T*-MoS_2 can be obtained through plasma bombardment [44], and the 1*T*' phase can be synthesized via a solution method [45]. Besides, the Janus MoSSe was successfully synthesized via the modified CVD method [27]. Therefore, it is believed that *H*-RuClBr and *H*-OsClBr could also potentially be prepared using similar CVD or plasma bombardment techniques.

The total energies with the FM configurations of *H*-RuClBr and *H*-OsClBr are 67.77 and 240.64 meV per unit cell lower than those with the AFM configuration, respectively, indicating the FM ground state of *H*-*M*ClBr (M = Ru, Os). The origin of ferromagnetism can be attributed to the superposition of the magnetic *M*-*M* direct exchange and *M*-Cl-*M* and *M*-Br-*M* superexchange interactions. Here the Ru-Cl-Ru (Os-Cl-Os) and Ru-Br-Ru (Os-Br-Os) bond angles are 88° (85°) and 83° (81°), both of which are close to 90°, suggesting that Ru 4d and Os 5d orbitals are nearly orthogonal to the Cl 3p and Br 4p orbitals. Meanwhile, the MAEs of *H*-RuClBr and *H*-OsClBr are calculated as MAE = E_θ–E_z, in which E_θ and E_z denote the energy of the system with the magnetization along a given θ and [001] direction. The angular dependence of MAE (see Fig. S3 [42]) in *H*-RuClBr demonstrates that the easy axis tends to lie in the isotropic xy plane and reaches a maximum value of 1.932 meV per Ru atom. Interestingly, the easy magnetization axis of *H*-RuClBr can be easily switched to the out-of-plane direction by applying an external magnetic field or a compressive strain, as shown in Fig. 6(a). Therefore, the primary focus of this study lies in investigating the properties associated with its magnetization axis along the out-of-plane direction. It is worth noting that the magnetization axis of *H*-OsClBr prefers to align along the z direction, which facilitates the spontaneous generation of valley polarization. To ensure practical implementation in

spintronic devices, a high Curie temperature (T_C) is also significant for FM materials. The T_C of *H*-RuClBr and *H*-OsClBr are evaluated using Monte Carlo simulations as implemented in the VAMPIRE package, and the classical Heisenberg spin Hamiltonian of the system can be written as

$$H = -J\sum_{i,j} S_i \cdot S_j - A\sum_i \left(S_i^z\right)^2, \tag{1}$$

where S_i/S_j and S_i^z represent the spin vectors and spin components along the z axis, respectively. J and A denote the nearest-neighbor exchange parameter and magnetic anisotropy. By constructing a $2\times2\times1$ supercell, the total energies of the FM and AFM configurations can be written as

$$E_{FM} = E_0 - 6J - 2A, \tag{2}$$

$$E_{AFM} = E_0 + 2J - 2A \tag{3}$$

in which E_0 is the energy of the system without spin polarization. Then the nearest-neighbor exchange parameter J can be obtained by the energy difference between FM and AFM as follows:

$$J = \frac{(E_{AFM} - E_{FM})}{8}. \tag{4}$$

The J values calculated according to formula (4) are 16.94 and 60.16 meV for *H*-RuClBr and *H*-OsClBr, respectively. The T_C is determined by the temperature-dependent magnetization $m(T) = (1-T/T_C)^\beta$ and the peak value of the specific heat $C_V = (\langle U^2\rangle - \langle U\rangle^2)/k_BT^2$. As shown in Figs. S3(c) and S3(d) [42], the theoretically predicted T_C values of *H*-RuClBr and *H*-OsClBr monolayers are 220 and 830 K, respectively, which perform much higher than the T_C of other monolayers that have been reported experimentally, such as CrI_3 (45 K) [46], $CrGeTe_3$ (20 K), and $Cr_2Ge_2Te_6$ (30 K) [47].

B. Ferrovalley polarization in the *H*-*M*ClBr monolayer

As shown in Fig. 1(d) and Fig. S6(a) [42], the spin-polarized band structures of *H*-RuClBr and *H*-OsClBr monolayers exhibit distinct valley characteristics at both the K and $-K$ valleys when the spin-orbit coupling (SOC) effect is absent. Due to the intrinsic spin polarization, the bands of spin-up and spin-down channels are well separated, which automatically removes the time-reversal-symmetry constraint. The valence-band maximum (VBM) and conduction-band minimum (CBM) located at the K and $-K$ valleys are contributed by the spin-down channel, which forms a pair of degenerate valleys. Besides, *H*-RuClBr and *H*-OsClBr exhibit semiconducting characteristics with direct band gaps of around 502 and 671 meV at the PBE+U level, respectively. With the consideration of SOC, as shown in Fig. 1(e) and Fig. S6(b) [42], the degeneracy between the two energy valleys breaks and results in the valley polarization with the values of 247 and 150 meV, equivalent to applying a giant external magnetic field of ~2000 T to produce the same valley polarization in WSe_2 and $MoSe_2$, which are significantly larger than those of VSi_2P_4 (49.4 meV) [24], *H*-$FeCl_2$ (101 meV) [48], and Nb_3I_8 (107 meV) [49]. As a consequence, such large valley polarization characteristics of *H*-RuClBr and OsClBr highlight their potential in nonvolatile valleytronics applications. To elaborate on the origin of spontaneous valley polarization, we developed a basic model to illustrate the SOC term as follows [50–52]:

$$\hat{H} = \lambda\hat{S}\cdot\hat{L} = \hat{L}_z\hat{S}_z + \tfrac{1}{2}\hat{L}_+\hat{S}_- + \tfrac{1}{2}\hat{L}_-\hat{S}_+ = \hat{H}^0_{SO} + \hat{H}'_{SO}, \tag{5}$$

where

$$\begin{aligned}\hat{H}^0_{SO} &= \lambda\hat{S}_{z'}\left(\hat{L}_z\cos\theta + \frac{1}{2}\hat{L}_+e^{-i\phi}\sin\theta + \frac{1}{2}\hat{L}_-e^{+i\phi}\sin\theta\right)\\ &= \lambda\hat{S}_{z'}(\hat{L}_z\cos\theta + \hat{L}_x\sin\theta\cos\phi + \hat{L}_y\sin\theta\sin\phi),\\ \hat{H}'_{SO} &= \frac{\lambda}{2}(\hat{S}_{+'} + \hat{S}_{-'})(-\hat{L}_z\sin\theta + \hat{L}_x\cos\theta\cos\phi\\ &\quad + \hat{L}_x\cos\theta\sin\phi).\end{aligned}$$

Here $\hat{L}$ and $\hat{S}$ represent the orbital and spin angular momentum operators, respectively. $\hat{L}_+$ and $\hat{L}_-$ are defined as ladder operators, which can be represented by the equation $\hat{L}_\pm = \hat{L}_x \pm i\hat{L}_y$. $\hat{L}_x$, $\hat{L}_y$, and $\hat{L}_z$ are the three components of $\hat{L}$ in the (x, y, z) coordinate system. Likewise, $\hat{S}_{\pm'}$ is a ladder operator defined as $\hat{S}_{\pm'} = \hat{S}_{x'} \pm i\hat{S}_{y'}$. $\hat{S}_{x'}$, $\hat{S}_{y'}$, and $\hat{S}_{z'}$ are the three components of $\hat{S}$ in the (x', y', z') coordinate system. The interactions between the same spin states and opposite spin states are denoted by $\hat{H}^0_{SO}$ and $\hat{H}'_{SO}$, respectively. As shown in Fig. 1(e), the valleys in the conduction band of *H*-RuClBr arise from the same spin channel. Therefore, the interaction denoted by $\hat{H}'_{SO}$ can be disregarded. Since the magnetization axis is oriented along the out-of-plane direction, the expression for $\hat{H}^0_{SO}$ simplifies to

$$\hat{H}^0_{SO} = \lambda\hat{S}_{Z'}\hat{L}_z = -\lambda\hat{L}_z. \tag{6}$$

As depicted in Fig. 1(f), the K and $-K$ valleys of *H*-RuClBr in the conduction band primarily arise from the dominant contributions of the Ru d_{xy} and Ru $d_{x^2-y^2}$ orbitals. Wang *et al.* demonstrate that, by considering the orbital and wave vector symmetries at the K and $-K$ valleys, we can find [53]

$$\hat{C}_3[d_{x^2-y^2}, d_{xy}, d_{z^2}] = [d_{x^2-y^2}, d_{xy}, d_{z^2}]\begin{bmatrix} -\frac{1}{2} & \frac{\sqrt{3}}{2} & 0\\ -\frac{\sqrt{3}}{2} & -\frac{1}{2} & 0\\ 0 & 0 & 1\end{bmatrix}. \tag{7}$$

Then the appropriate basis functions of $|\varphi_c^\tau\rangle = \frac{1}{\sqrt{2}}(|d_{x^2-y^2}\rangle + \tau i|d_{xy}\rangle)$ and $|\varphi_v^\tau\rangle = |d_{z^2}\rangle$ are chosen, where $\tau = \pm1$ is used to denote the K and $-K$ valley indices. Furthermore, the energy levels of these valleys can be represented by $E^\tau = \langle\varphi^\tau|\hat{H}^0_{SO}|\varphi^\tau\rangle$. Thus, the valley polarization observed in the conduction band and valence band can be represented by

$$\begin{aligned}E_c^K - E_c^{-K} &= i\left(\langle d_{x^2-y^2}|\hat{H}^0_{SO}|d_{xy}\rangle - \langle d_{xy}|\hat{H}^0_{SO}|d_{x^2-y^2}\rangle\right)\\ &= -i\lambda\left(\langle d_{x^2-y^2}|\hat{L}_z|d_{xy}\rangle - \langle d_{xy}|\hat{L}_z|d_{x^2-y^2}\rangle\right)\\ &= -i\lambda(-2i - 2i) = -4\lambda,\end{aligned} \tag{8}$$

$$E_v^K - E_v^{-K} = i\left(\langle d_{z^2}|\hat{H}^0_{SO}|d_{z^2}\rangle - \langle d_{z^2}|\hat{H}^0_{SO}|d_{z^2}\rangle\right) = 0, \tag{9}$$

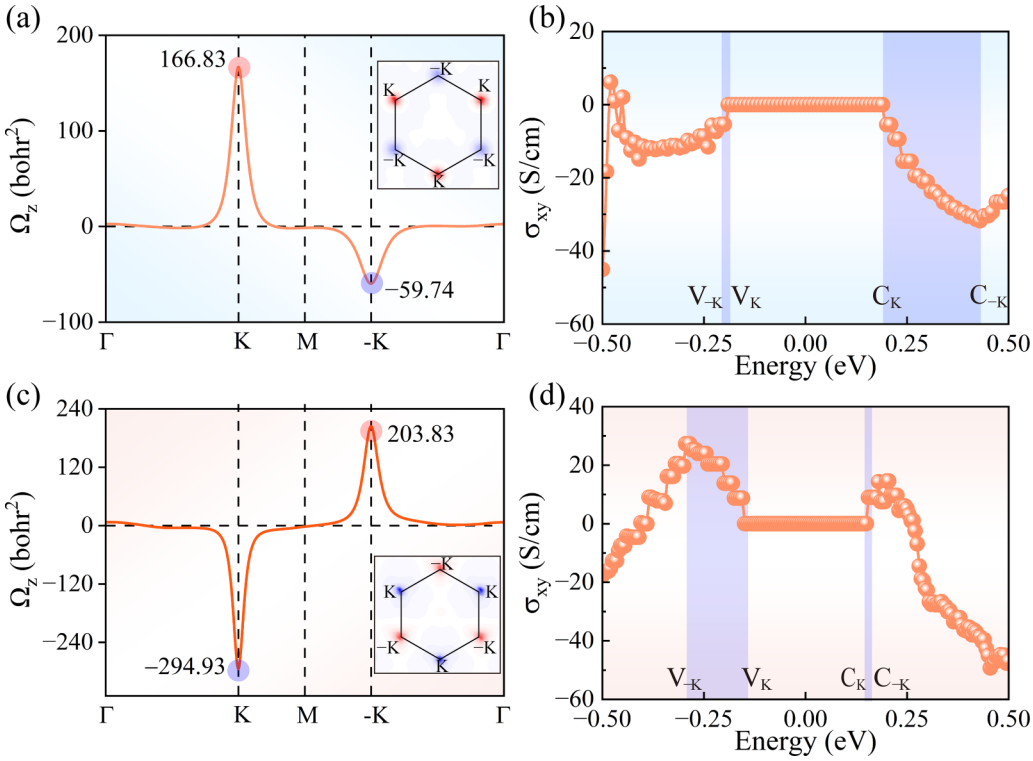

FIG. 2. Berry curvature $\Omega_z(k)$ of (a) H-RuClBr and (c) H-OsClBr along the high-symmetry points. Insets are the Berry curvature over the whole 2D Brillouin zone. [(b) and (d)] The anomalous Hall conductivities. C_K (V_K) and C_{-K} (V_{-K}) refer to the conduction-band minimum (valence-band maximum) in the K and $-K$ valleys. The dark and light blue regions in Figs. 3(a) and 3(b) represent the state with and without valley polarization.

where $\hat{L}_z|d_{xy}\rangle = -2i|d_{x^2-y^2}\rangle$ and $\hat{L}_z|d_{x^2-y^2}\rangle = 2i|d_{xy}\rangle$. As first-order perturbations in the SOC effect, the above analysis confirms that the valley in the valence band remains degenerate, whereas the valley in the conduction band is lifted, leading to a large valley polarization, which is consistent with first-principles calculations.

Due to the intrinsic inversion symmetry breaking of H-RuClBr and H-OsClBr, the charge carriers at different valleys will generate a valley-contrasting Berry curvature and AVHE raised from the valley polarization. The Berry curvatures of H-RuClBr and H-OsClBr in the occupied states can be expressed as

$$\Omega_z(k) = \sum_n f_n \Omega_n(k) \tag{10}$$

and

$$\Omega_n(k) = -\sum_{n\neq m} \frac{2\mathrm{Im}\langle\psi_{nk}|v_x|\psi_{mk}\rangle\langle\psi_{mk}|v_y|\psi_{nk}\rangle}{[E_n(k) - E_m(k)]^2}, \tag{11}$$

based on the Kubo formula [54]. The symbol f_n represents the Fermi-Dirac distribution function, while $v_{x(y)}$ denotes the velocity operator along the $x(y)$ direction. The Bloch wave function with eigenvalue E_n is represented by ψ_{nk}. The Berry curvature $\Omega_z(k)$ of H-RuClBr along its high-symmetry points at 0 K is shown in Fig. 2(a). Notably, two prominent peaks appear at the $+K$ ($\Omega_K = 166.83$ bohr^2) and $-K$ ($\Omega_{-K} = -59.74$ bohr^2) valleys. A similar result also appears in H-OsClBr with the Berry curvature values of $\Omega_K = -294.93$ bohr^2 and $\Omega_{-K} = 203.83$ bohr^2 in Fig. 2(c) at 0 K. Simultaneously, the distribution of $\Omega_n(k)$ in the whole 2D Brillouin zone, as illustrated in the insets of Figs. 2(a) and 2(c), reveals the C_3 symmetry of the system and the extreme Berry curvature values at K and $-K$ valleys. As expected, $\Omega_n(k)$ exhibits opposite signs at two valleys owing to the absence of inversion symmetry, which evidences the robust valley-contrasting feature in H-RuClBr and H-OsClBr. Interestingly, the Berry curvature of H-RuClBr and H-OsClBr at the K valley also shows an inverse sign, which is discussed in detail in Sec. III D. In this case, the nonzero $\Omega_n(k)$ can serve as an effective magnetic field in the presence of an in-plane longitudinal electric field E on the Bloch electrons, thus endowing the charge carriers with an anomalous transverse velocity of

$$\upsilon = -\frac{e}{\hbar} E \times \Omega_n(k). \tag{12}$$

The Fermi level of H-RuClBr and H-OsClBr can be shifted between the K and $-K$ valleys of the conduction and valence bands through charge doping and hole doping, respectively. At this time, in the case of n-type RuClBr, the spin-down electrons originating from the K valley will induce a transverse velocity as a result of conduction valley polarization. In the case of p-type H-OsClBr, as valley polarization manifests in the valence band, the spin-down holes stemming from the K valley will similarly experience a transverse velocity. Thus, there is a net accumulation of carriers on one side of H-RuClBr and H-OsClBr under an in-plane longitudinal elec-

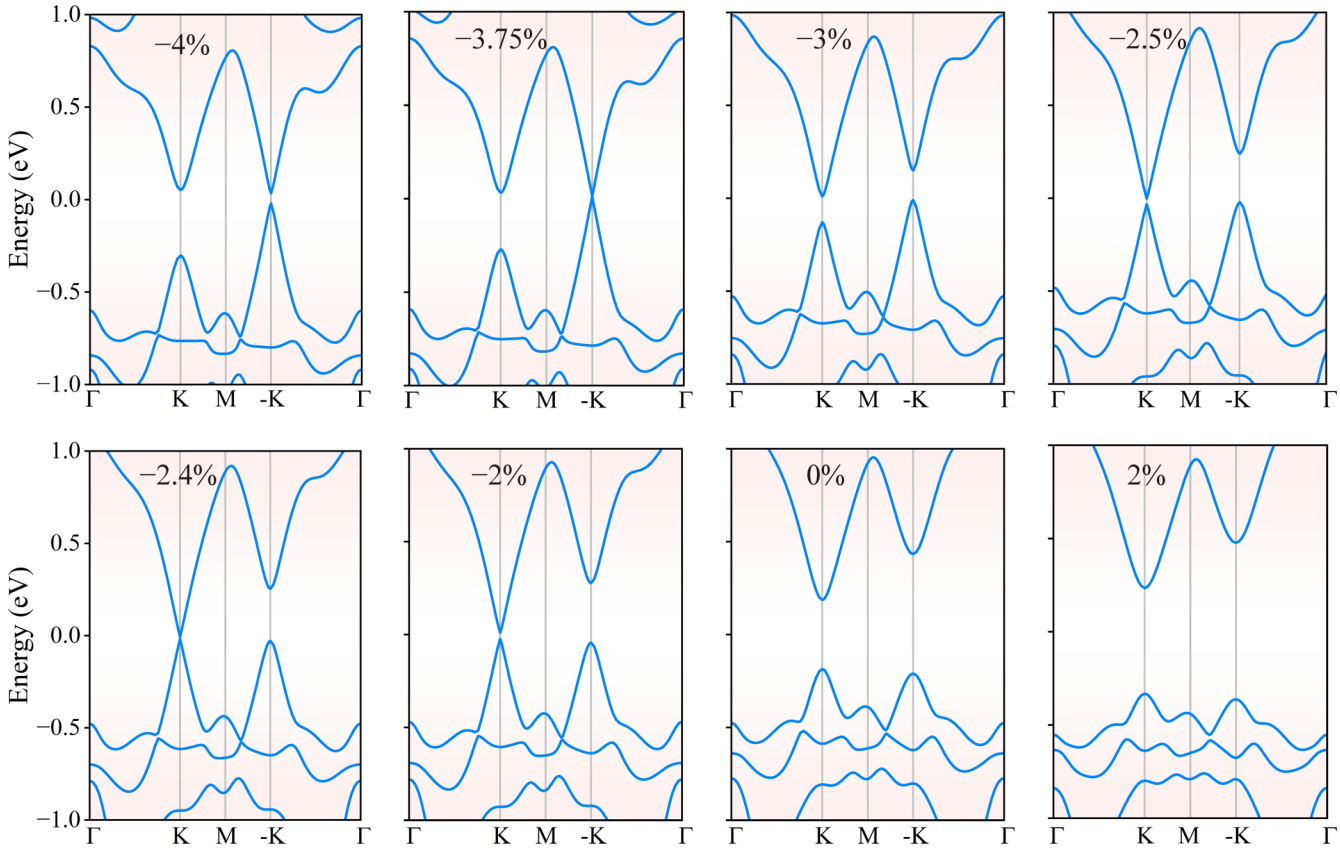

FIG. 3. The electronic band structures of RuClBr under different strains.

tric field, resulting in a net Hall current along the transversal direction, namely, the anomalous valley Hall effect as illustrated in Fig. 5(c). To validate this hypothesis, we further calculate the anomalous Hall conductivity by

$$\sigma_{xy} = -\frac{e^2}{\hbar}\int \frac{d^2k}{(2\pi)^2}\Omega_n(k). \tag{12}$$

As the Fermi energy level shifts between the K and $-K$ valleys in the valence band and conduction band, a nonzero value of σ_{xy} is observed, as depicted by a marked shadow in Figs. 2(b) and 2(d). The disparity in $\Omega_n(k)$ between the K and $-K$ valleys leads to an accumulation of spin-down holes from the K valley on one side of the sample, leading to the generation of the AVHE. Since the net accumulated hole carriers originate from the same valley channel, the transversal charge, spin, and valley Hall currents generate simultaneously, facilitating the detection of valley pseudospin and practical valleytronic applications.

C. Topological band transition in the *H*-*M*ClBr monolayer

Given the fact that any 2D materials inevitably suffer structural modification during the synthesis process on the substrate, it is thus mandatory to evaluate the effect of in-plane strain on the magnetic and electronic properties of *H*-RuClBr and *H*-OsClBr monolayers for their practical applications in spintronics and valleytronics. In this work, the in-plane strain ε within $\pm 5\%$, defined as $\varepsilon = (a–a_0)/a_0$, is applied, where a and a_0 are the lattice constants of *H*-RuClBr and *H*-OsClBr in the unstrained and strained states, respectively. To confirm the structural stabilities of *H*-RuClBr and *H*-OsClBr under strain state, we calculate the phonon spectra under different strains as shown in Fig. S7 [42]. It is observed that, within the studied strain range, both *H*-RuClBr and *H*-OsClBr exhibit no imaginary frequencies in their phonon spectra, demonstrating their dynamic stabilities under various strains and suggesting their potential in van der Waals heterostructure applications. As shown in Figs. S10 and S11 [42], the magnetic ground states of *H*-RuClBr and *H*-OsClBr remain FM under different biaxial strains. As the tensile strain increases, the MAE of *H*-RuClBr decreases continuously. The band structures of *H*-RuClBr, as affected by strain, are illustrated in Fig. 3, respectively. The valley polarization undergoes a significant transition from the conduction band to the valence band when the applied compressive strain exceeds 3.75%. In contrast, the valley polarization remains unaltered at the tensile strain. The band structure of *H*-OsClBr also exhibits significant alterations under different strains, as shown in Fig. S8 [42].

Through the above analysis, it was determined that the space group of *H*-MClBr is $P\bar{3}m1$ with a corresponding point group of D_3. The valley Chern number C_{+K}/C_{-K} is defined as the integral over half of the Brillouin zone, where the $K/-K$ valley is located [55,56]. For *H*-RuClBr, we obtain $C_{\text{tot}} = 0$ and $C_{+K} = 1$ ($C_{-K} = -1$), indicating a total valley Chern number $C_v = 2$ and suggesting the presence of a quantum valley Hall effect in the system. The combined symmetry indicators at the K and $-K$ valleys are $(1, D_3)$ and $(-1, D_3)$, respectively, implying distinct symmetries between K and $-K$

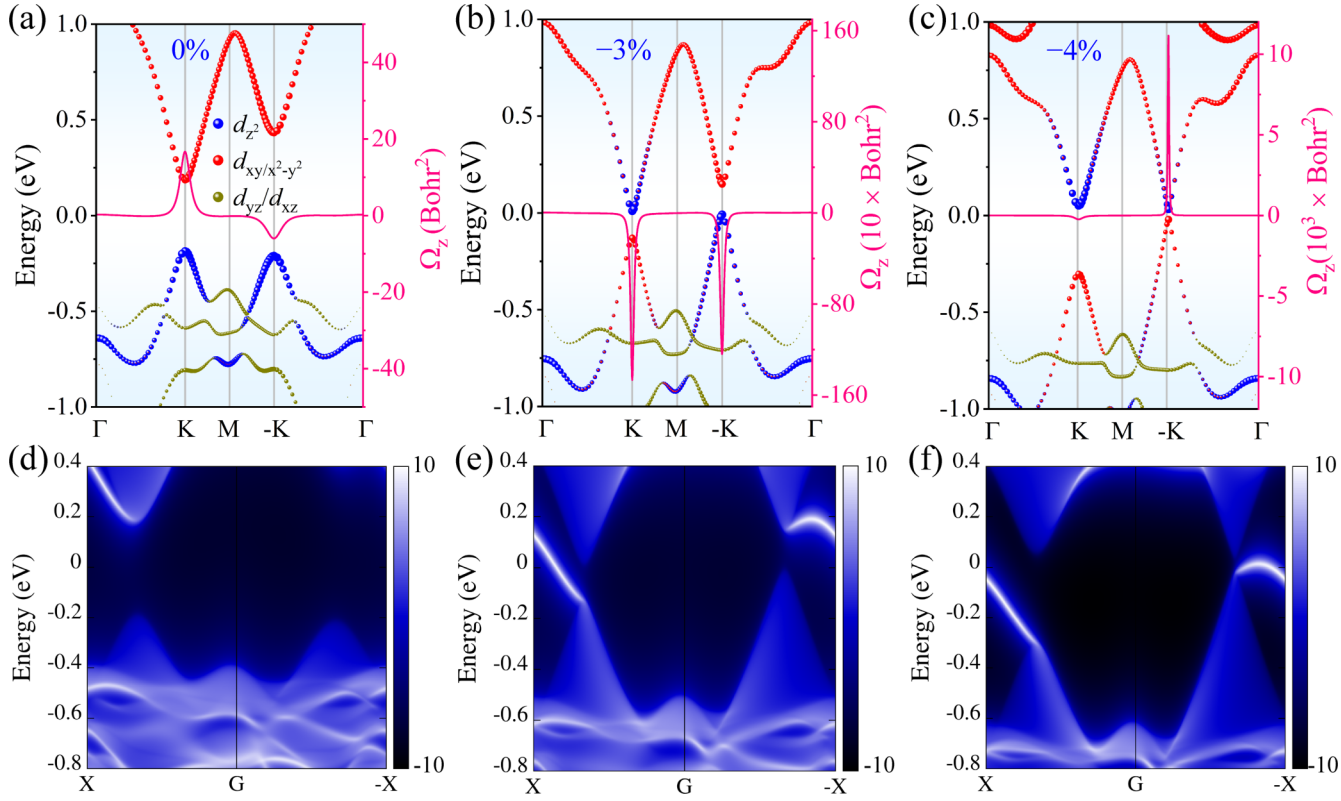

FIG. 4. Orbital-resolved band structures and corresponding Berry curvatures of *H*-RuClBr under different strains of (a) 0%, (b) −3%, and (c) −4%. The topological edge states of RuClBr under corresponding strains of (d) 0%, (e) −3%, and (f) −4%.

valleys and anticipating a topological phase transition. Additionally, we employ the $k \cdot p$ Hamiltonian model to elucidate the band inversion, as elaborated in Sec. III D. As shown in Figs. 5(a) and 5(b), it becomes evident that, as the compressive strain of 2.4% is applied to *H*-RuClBr, the band gap at the *K* valley vanishes, while a band gap of 0.28 eV persists at the $-K$ valley, thus leading to the HVM state. When the compressive strain further increases to 3.75%, the band gap

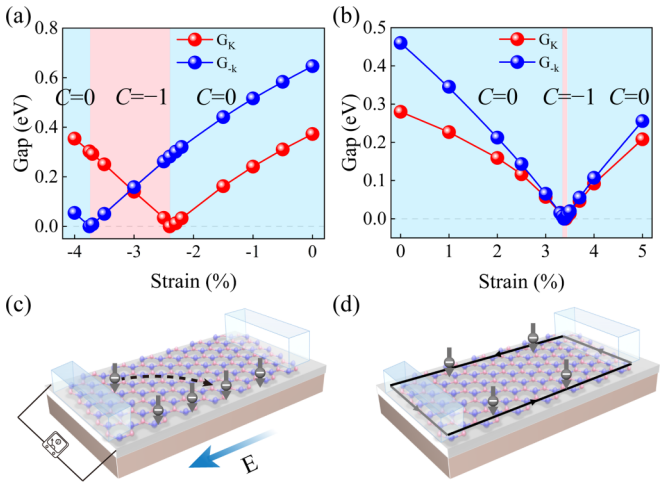

FIG. 5. The band gaps at *K* and $-K$ valleys of (a) *H*-RuClBr and (b) *H*-OsClBr under different strains. The red lines and blue lines represent the band gaps at the *K* and $-K$ valleys, respectively. [(c) and (d)] The schematic diagrams of AVHE and VQAHE, respectively.

at the $-K$ valley vanishes, while a new gap of 0.3 eV emerges at the *K* valley. The characteristic of band gap closing and reopening leads to a band inversion, resulting in the topological band phase transition. As shown in Fig. 4(a), in the absence of strain, the VBM and CBM of *H*-RuClBr are primarily contributed by the d_{z^2} and $d_{xy}/d_{x^2-y^2}$ orbitals, respectively. In Fig. 4(b), it is evident that band inversion occurs at the *K* valley when the compressive strain varies from 2.4% to 3.75%. To validate the presence of the topological state, we calculate the Berry curvature and edge states of *H*-RuClBr under different compressive strains. As depicted in Figs. 4(b) and 4(e), at a compressive strain of 3%, the Berry curvatures at the *K* and $-K$ valleys are both negative, accompanied by the emergence of a chiral edge state, which connects the conduction and valence bands. This observation aligns with the characteristic features of the quantum anomalous Hall (QAH) state, as shown in Fig. 5(d). By integrating the Berry curvature over the first Brillouin zone, a Chern number of −1 is obtained, providing evidence for the existence of a nontrivial topological state. When compressive strain exceeds 3.75%, another band inversion occurs at the $-K$ valley, as shown in Fig. 4(c). The band gaps at *K* and $-K$ valleys reappear and the edge states vanish, indicating that *H*-RuClBr becomes topologically trivial.

Similarly, it is shown that *H*-OsClBr is initially topologically trivial without any applied biaxial strain. Nonetheless, at tensile strains of 3.38% and 3.415%, the band gaps of *H*-OsClBr close at the *K* and $-K$ valleys, respectively, as illustrated in Fig. S18 [42]. When the tensile strain is between 3.38% and 3.415%, band inversion occurs at the $-K$

valley, while the band at the K valley remains topologically trivial. The presence of negative Berry curvature at both the K and $-K$ valleys, along with the emergence of edge states connecting the conduction and valence bands, confirms the emergence of a nontrivial topological state connecting the conduction and valence bands, and confirms the emergence of a nontrivial state. As shown in Figs. S9(c) and S9(f) [42], when the tensile strain further increases to over 3.415%, the Berry curvature at K and $-K$ valleys exhibits an inverse sign, and the edge state vanishes, indicating that H-OsClBr also undergoes a transition to a topologically trivial state. Thus, by applying biaxial strain within 2D Janus magnetic transition metal dihalides, it becomes feasible to transition between the anomalous valley Hall and valley-polarization QAH states. This finding offers great potential in novel application for the interplay among valleytronics, spintronics, and band topology.

D. The $k \cdot p$ model

To better understand the Berry curvature difference and topological phase transitions in H-RuClBr and H-OsClBr, we construct a two-band $k \cdot p$ Hamiltonian model:

$$H_0 = at\left(\tau k_x \hat{\sigma}_x + k_y \hat{\sigma}_y\right) + \frac{\Delta}{2}\hat{\sigma}_z + \varepsilon \hat{\sigma}_0, \tag{13}$$

in which a, t, τ, and Δ are the lattice constant, effective nearest-neighbor hopping, valley index, and energy gap, respectively. $\hat{\sigma}$ represents the Pauli matrices for two basic functions, and ε is the on-site energy. The total Hamiltonian of hexagonal ferromagnetic lattices under small biaxial strain [18,57], accounting for exchange interactions and SOC, can be expressed by

$$\begin{aligned} H =& H_0 + \lambda_c \tau \hat{s}_z \frac{\hat{\sigma}_z + \hat{\sigma}_0}{2} + \lambda_v \tau \hat{s}_z \frac{\hat{\sigma}_z - \hat{\sigma}_0}{2} \\ & - \hat{s}_z \frac{m_1 \hat{\sigma}_z + m_2 \hat{\sigma}_0}{2} + (f_1 \hat{\sigma}_z - f_2 \hat{\sigma}_0)(\varepsilon_{xx} + \varepsilon_{yy}). \end{aligned} \tag{14}$$

Thus, the total Hamiltonian can be described as

$$H = \begin{bmatrix} \frac{\Delta}{2} + \varepsilon + \hat{s}_z \lambda_c \tau - \hat{s}_z m_c + 2(f_1 - f_2)\varepsilon_{xx} & at(\tau k_x - k_y) \\ at(\tau k_x + k_y) & -\frac{\Delta}{2} + \varepsilon + \hat{s}_z \lambda_v \tau - \hat{s}_z m_v - 2(f_1 + f_2)\varepsilon_{xx} \end{bmatrix}. \tag{15}$$

Here, $\lambda_{c(v)}$ and $m_{c(v)}$ ($m_c = \frac{m_1+m_2}{2}$, $m_v = \frac{m_1-m_2}{2}$) represent the spin splitting caused by the SOC effect and the effective exchange splitting at the conduction-band minimum and the valence-band maximum, respectively. A spin index with $+1$ (-1) denotes the spin-up (spin-down) state. f_1 and f_2 are band-gap adjustment parameters. The Berry curvature can be rewritten as [55]

$$\Omega_n(k) = \sum_{n \neq m} \frac{i\left(\langle \psi_{nk}|\frac{\partial H}{\partial k_x}|\psi_{mk}\rangle\langle\psi_{mk}|\frac{\partial H}{\partial k_y}|\psi_{nk}\rangle - \langle \psi_{nk}|\frac{\partial H}{\partial k_y}|\psi_{mk}\rangle\langle\psi_{mk}|\frac{\partial H}{\partial k_x}|\psi_{nk}\rangle\right)}{[E_n(k) - E_m(k)]^2}. \tag{16}$$

Only the first term of the H_0 Hamiltonian is dependent on the wave vector. In combination of Eqs. (13) and (16), we can finally obtain that $\Omega_n(k) \propto -\langle\psi_v|t(k)|\psi_c\rangle\langle\psi_c|t(k)|\psi_v\rangle$. Here $\langle\psi_v|t(k)|\psi_c\rangle$ and $\langle\psi_c|t(k)|\psi_v\rangle$ are not necessarily conjugate for a given k, and this is exactly what endows the physical degree of freedom to reverse the Berry curvature because $\langle\psi_v|t(k)|\psi_c\rangle\langle\psi_c|t(k)|\psi_v\rangle$ is not always positive. The final result we obtained from WANNIER90 is shown in Table I, and it qualitatively agrees with the Berry curvature shown in Fig. 2. The Berry curvatures of H-RuClBr and H-OsClBr exhibit opposite trends, both with larger peaks near the K valley and smaller reversed peaks near the $-K$ valley.

Furthermore, this two-band $k \cdot p$ Hamiltonian model can also explain the topological phase transitions in H-RuClBr and H-OsClBr. For the spin-down channel, by diagonalizing the total Hamiltonian, we obtain the energy spectra with

$$\begin{aligned} E(\psi^\tau) =& \varepsilon + \tau\frac{\lambda_v - \lambda_c}{2} + \frac{m_2}{2} - 2f_2\varepsilon_{xx} \\ & \pm \sqrt{(\Delta')^2 + a^2t^2\left(k_x^2 + k_y^2\right)}, \end{aligned} \tag{17}$$

where $\Delta' = \frac{\Delta - \tau(\lambda_v + \lambda_c) + m_1 + 4f_1\varepsilon_{xx}}{2}$. The band gap at K and $-K$ valleys can be expressed as $E_g = \Delta - \tau(\lambda_v + \lambda_c) + m_1 + 2f_1\varepsilon_{xx}$. As the compressive strain increases, the band gap at the K ($\tau = 1$) valley decreases to zero, while the band gap at the $-K$ ($\tau = -1$) valley remains greater than zero, leading to a band inversion occurring at the K valley.

TABLE I. The $-\langle\psi_v|t(k)|\psi_c\rangle\langle\psi_c|t(k)|\psi_v\rangle$ values at K and $-K$ valleys for H-RuClBr and H-OsClBr (in 10^{-6} eV^2).

System	K	$-K$
H-RuClBr	32.544	−0.014
H-OsClBr	−0.210	0.123

E. MAE origin and strain manipulation

For ferrovalley materials, the out-of-plane alignment of the magnetic moment is the prerequisite for inducing spontaneous valley polarization. Fortunately, even under the significant tensile strain of up to 5%, H-OsClBr exhibits a consistently positive MAE, indicating its robust perpendicular magnetocrystalline anisotropy as shown in Fig. 6(b). On the other hand, as the compressive strain gradually increases, there is a transition of MAE from negative to positive at a compressive strain of approximately −3% in H-RuClBr, as illustrated in Fig. 6(a). This indicates that the easy magnetization axis

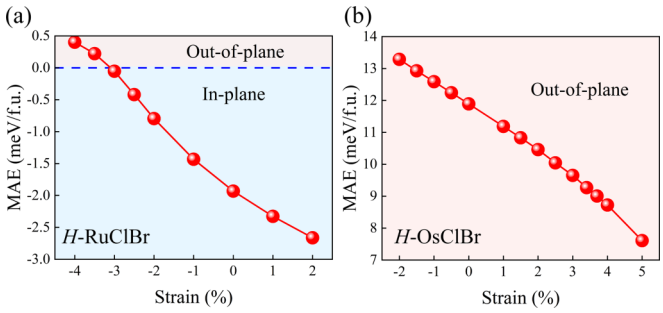

FIG. 6. MAE evolution of (a) *H*-RuClBr and (b) *H*-OsClBr under different strains.

undergoes a transition from the in-plane to the out-of-plane direction. To further unveil the easy magnetization origin and manipulation of *H*-RuClBr and *H*-OsClBr, we calculate the orbital-resolved MAE by considering the second-order perturbation, in which the *d*-orbital hybridization determines the MAE as follows [58]:

$$\begin{aligned}\mathrm{MAE} &= \sum_{\sigma\sigma'} E^{\sigma\sigma'}(100) - E^{\sigma\sigma'}(001) \\ &= \xi^2 \sum_{\sigma,\sigma',u,o} (-1)^{1-\delta_{\sigma\sigma'}} \\ &\times \left[\frac{\langle o^{\sigma'}|\hat{L}_z|u^{\sigma}\rangle^2 - \langle o^{\sigma'}|\hat{L}_x|u^{\sigma}\rangle^2}{\varepsilon_u^{\sigma} - \varepsilon_o^{\sigma'}} \right], \end{aligned} \tag{18}$$

where ξ stands for the SOC constant, $\hat{L}_z$ and $\hat{L}_x$ are the orbital angular momentum operators, and o, u, and δ represent the occupied, unoccupied, and Kronecker function, respectively. The symbols σ and σ' denote spin states, which are restricted to the values of 1 (spin up) or -1 (spin down). ε_u^{σ} and $\varepsilon_o^{\sigma'}$ are the energies of unoccupied states with σ spin and occupied states with σ' spin. In fact, by considering the distinct spin states of occupied and unoccupied orbitals, the MAE can be decomposed into four components:

$$\begin{aligned}\mathrm{MAE} &= E_{1,1} + E_{-1,-1} + E_{1,-1} + E_{-1,1}, \\ E_{1,1} &= \xi^2 \frac{|\langle o^1|\hat{L}_z|u^1\rangle|^2 - |\langle o^1|\hat{L}_x|u^1\rangle|^2}{\varepsilon_u^1 - \varepsilon_o^1}, \\ E_{-1,-1} &= \xi^2 \frac{|\langle o^{-1}|\hat{L}_z|u^{-1}\rangle|^2 - |\langle o^{-1}|\hat{L}_x|u^{-1}\rangle|^2}{\varepsilon_u^{-1} - \varepsilon_o^{-1}}, \\ E_{1,-1} &= -\xi^2 \frac{|\langle o^1|\hat{L}_z|u^{-1}\rangle|^2 - |\langle o^1|\hat{L}_x|u^{-1}\rangle|^2}{\varepsilon_u^{-1} - \varepsilon_o^1}, \\ E_{-1,1} &= -\xi^2 \frac{|\langle o^{-1}|\hat{L}_z|u^1\rangle|^2 - |\langle o^{-1}|\hat{L}_x|u^1\rangle|^2}{\varepsilon_u^1 - \varepsilon_o^{-1}}. \end{aligned} \tag{19}$$

To ascertain the dominant factor influencing the change in MAE under strain, we analyzed the MAE distribution within the Brillouin zone both in unstrained conditions and at a compressive strain of -4%, as illustrated in Fig. 7 and Fig. S12 [42]. As shown in Figs. 7(b) and 7(c) and Figs. S12(b) and S12(c) [42], the combined effects of the two spin-conservation terms ($E_{1,1}$ and $E_{-1,-1}$) tend to mutually offset each other

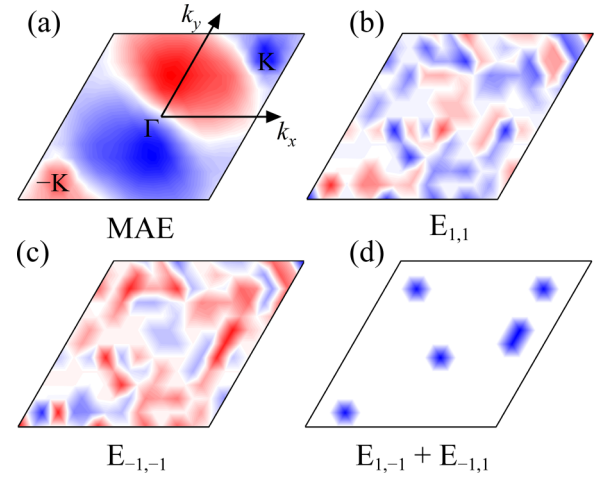

FIG. 7. (a) Total MAE in the first Brillouin zone for *H*-RuClBr. MAE contributed by the spin-conservation terms (b) $E_{1,1}$ and (c) $E_{-1,-1}$. (d) MAE contributed by the spin-flip terms ($E_{1,-1}$ and $E_{-1,1}$). The red and blue regions represent the positive and negative values.

in scenarios with no strain and under a compressive strain of -4%. In other words, the two spin-flip terms ($E_{1,-1}$ and $E_{-1,1}$) significantly contribute to the magnetization axis transformation of *H*-RuClBr from in plane to out of plane under strain conditions, as illustrated in Fig. 7(d) and Fig. S12(d) [42]. Thus, in the analysis of strain-induced changes in MAE, our primary focus is on two spin-flip terms.

The *s* and *p* orbitals are disregarded due to the dominance of Ru *d* orbitals at the Fermi level. Based on the analysis of Figs. 8(a) and 8(b), it is evident that the variation in MAE with strain primarily arises from alterations in matrix elements ($d_{x^2-y^2}$ and d_{xy}) and (d_{z^2} and d_{yz}), wherein the former predominantly contributes to negative MAE while the latter contributes to positive MAE. As depicted in Fig. 8(c), the e_1 orbitals (d_{xy} and $d_{x^2-y^2}$) are degenerate, with their predominant distribution observed in the occupied spin-up and unoccupied spin-down channels of the *d* orbitals. From Table SI [42], we can obtain

$$\Delta E = -\xi^2 \frac{4}{\varepsilon^{-1}_{d_{x^2-y^2}/d_{xy}} - \varepsilon^{1}_{d_{x^2-y^2}/d_{xy}}}. \tag{20}$$

For the (d_{z^2} and d_{yz}) matrix element, the d_{z^2} matrix element is predominantly localized in the unoccupied spin-down channel, while the d_{yz} matrix element is primarily distributed in the occupied spin-up channel. From Table SI [42], we obtain

$$\Delta E = \xi^2 \frac{3}{\varepsilon^{-1}_{d_{z^2}} - \varepsilon^{1}_{d_{yz}}}. \tag{21}$$

As the compressive strain increases to -4%, The energy difference between $\varepsilon^{-1}_{d_{x^2-y^2}/d_{xy}}$ and $\varepsilon^{1}_{d_{x^2-y^2}/d_{xy}}$ increases from pristine 1.61 eV to 2.078 eV. According to Eq. (20), this change leads to a reduction in the contribution of negative MAE, as depicted in Fig. 8(d). Simultaneously, the energy difference between $\varepsilon^{-1}_{d_{z^2}}$ and $\varepsilon^{1}_{d_{yz}}$ decreases from pristine 0.73 eV to 0.63 eV, thereby enhancing the contribution of (d_{z^2}, d_{yz}) towards positive MAE according to Eq. (21), as shown in Fig. 8(d). Furthermore, assuming that the majority spin is

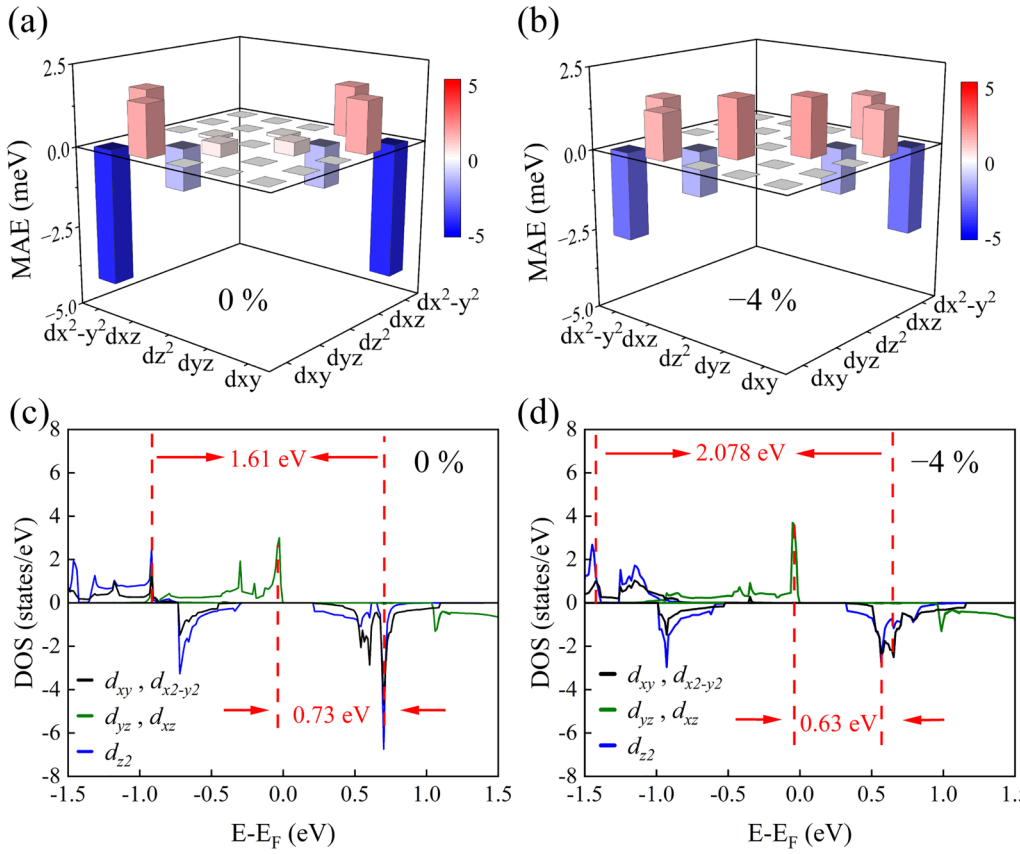

FIG. 8. Orbital-resolved single-ion anisotropy energy of Ru atom for *H*-RuClBr at (a) 0% strain and (b) −4% strain. Projected density of states (DOS) of Ru *d* orbitals at (c) 0% strain and (d) −4% strain. The difference between the two vertical red lines represents the energy difference between $\varepsilon^{-1}_{d_{x^2-y^2}/d_{xy}} - \varepsilon^{1}_{d_{x^2-y^2}/d_{xy}}$ and $\varepsilon^{-1}_{d_{z^2}} - \varepsilon^{1}_{d_{yz}}$.

fully occupied, the following formula can be derived based on Eq. (18) [59]:

$$\mathrm{MAE} = -\frac{\xi\hbar}{4\mu_{\mathrm{B}}}\sum(\mu_{l,\parallel} - \mu_{l,\perp}), \tag{22}$$

where $\mu_{l,\parallel}$ and $\mu_{l,\perp}$ denote the components of orbital moment along the in-plane and out-of-plane spin magnetization directions, respectively. In the absence of strain, with $\mu_{l,\parallel} = 0.094\,\mu_{\mathrm{B}}$ and $\mu_{l,\perp} = 0.061\,\mu_{\mathrm{B}}$, the negative MAE value suggests that the magnetic moment is oriented along the in-plane direction. However, under a compressive strain of −4%, where $\mu_{l,\parallel} = 0.084\,\mu_{\mathrm{B}}$ and $\mu_{l,\perp} = 0.087\,\mu_{\mathrm{B}}$, the positive MAE value indicates a change in the magnetization direction out of plane. Consequently, under a compressive strain of −4%, a transition from negative to positive MAE and the out-of-plane magnetization axis is realized in *H*-RuClBr. Thus, by strain engineering, it is expected that the easy magnetization axis of both *H*-RuClBr and *H*-OsClBr can be manipulated to the out-of-plane direction, offering an applicable approach to modulate the MAE in 2D materials, which facilitates the emergence of spontaneous valley polarization and the manifestation of topological states.

IV. CONCLUSION

In summary, by using the first-principles calculations and a tight-binding model, a comprehensive analysis is conducted on the magnetic, electronic, and valleytronic characteristics of the 2D Janus magnetic transition metal dihalides, *H*-RuClBr and *H*-OsClBr, with the valley-polarized band topological phase transition and perpendicular magnetocrystalline anisotropy via strain manipulation. It is discovered that spontaneous valley polarization could be realized in *H*-RuClBr and *H*-OsClBr with the values of 247 and 150 meV, respectively, which exceed those of most reported 2D ferrovalley materials. Moreover, *H*-OsClBr favors a pristine out-of-plane magnetization, while the easy magnetization axis of *H*-RuClBr could be switched from the in-plane to the out-of-plane direction via a compressive strain. The MAE of *H*-RuClBr and *H*-OsClBr is mainly contributed by different spin channels in the *d* orbitals of Ru and Os. Notably, the transition from anomalous valley Hall effect to a nontrivial topological state in both *H*-RuClBr and *H*-OsClBr is also observed under the biaxial strain. Besides, a two-band $k \cdot p$ model is constructed to illustrate the Berry curvature difference and topological phase transitions. Our work expands applications for the interplay among valleytronics, spintronics, and band topology in 2D Janus magnetic transition metal dihalides.

ACKNOWLEDGMENTS

This work was supported by the National Key Research and Development Program of China (Grant No.

2022YFA1204004), the National Natural Science Foundation of China (Grants No. 52201288, No. 52130103, and No. 12374099), China Postdoctoral Science Foundation (Grant No. 2023T160046), and the Fundamental Research Funds for the Central Universities (Grant No. 06500237).

The authors declare no competing financial interest.

[1] A. Rycerz, J. Tworzydło, and C. W. J. Beenakker, Valley filter and valley valve in graphene, Nat. Phys. **3**, 172 (2007).

[2] D. Xiao, W. Yao, and Q. Niu, Valley-contrasting physics in graphene: Magnetic moment and topological transport, Phys. Rev. Lett. **99**, 236809 (2007).

[3] Z. Zhu, A. Collaudin, B. Fauqué, W. Kang, and K. Behnia, Field-induced polarization of Dirac valleys in bismuth, Nat. Phys. **8**, 89 (2012).

[4] D. Xiao, G.-B. Liu, W. Feng, X. Xu, and W. Yao, Coupled spin and valley physics in monolayers of MoS_2 and other group-VI dichalcogenides, Phys. Rev. Lett. **108**, 196802 (2012).

[5] T. Cao *et al.*, Valley-selective circular dichroism of monolayer molybdenum disulphide, Nat. Commun. **3**, 887 (2012).

[6] J. Zhao, T. Zhang, R. Peng, Y. Dai, B. Huang, and Y. Ma, Spontaneous valley polarization and electrical control of valley physics in single-layer $TcIrGe_2S_6$, J. Phys. Chem. Lett. **13**, 8749 (2022).

[7] S. Shrestha, M. Li, S. Park, X. Tong, D. DiMarzio, and M. Cotlet, Room temperature valley polarization via spin selective charge transfer, Nat. Commun. **14**, 5234 (2023).

[8] W.-T. Hsu *et al.*, Negative circular polarization emissions from $WSe_2/MoSe_2$ commensurate heterobilayers, Nat. Commun. **9**, 1356 (2018).

[9] J. Liu, W.-J. Hou, C. Cheng, H.-X. Fu, J.-T. Sun, and S. Meng, Intrinsic valley polarization of magnetic VSe_2 monolayers, J. Phys.: Condens. Matter **29**, 255501 (2017).

[10] C. Zhang, Y. Nie, S. Sanvito, and A. Du, First-principles prediction of a room-temperature ferromagnetic Janus VSSe monolayer with piezoelectricity, ferroelasticity, and large valley polarization, Nano Lett. **19**, 1366 (2019).

[11] C. Luo, X. Peng, J. Qu, and J. Zhong, Valley degree of freedom in ferromagnetic Janus monolayer H-VSSe and the asymmetry-based tuning of the valleytronic properties, Phys. Rev. B **101**, 245416 (2020).

[12] S. Li, Q. Wang, C. Zhang, P. Guo, and S. A. Yang, Correlation-driven topological and valley states in monolayer VSi_2P_4, Phys. Rev. B **104**, 085149 (2021).

[13] M. Abdollahi and M. Bagheri Tagani, Janus 2H-VSSe monolayer: Two-dimensional valleytronic semiconductor with non-volatile valley polarization, J. Phys.: Condens. Matter **34**, 185702 (2022).

[14] H. Zhang, W. Yang, Y. Ning, and X. Xu, Abundant valley-polarized states in two-dimensional ferromagnetic van der Waals heterostructures, Phys. Rev. B **101**, 205404 (2020).

[15] F. Zhan, B. Zheng, X. Xiao, J. Fan, X. Wu, and R. Wang, Magnetic field induced valley-polarized quantum anomalous Hall effects in ferromagnetic van der Waals heterostructures, Phys. Rev. B **105**, 035131 (2022).

[16] X. Feng, L. Cai, Z. Chen, Y. Dai, B. Huang, and C. Niu, Tunable second-order topological insulators in Chern insulators 2H-FeX_2 (X = Cl and Br), Appl. Phys. Lett. **122**, 193104 (2023).

[17] Y. Wu, J. Tong, L. Deng, F. Luo, F. Tian, G. Qin, and X. Zhang, Realizing spontaneous valley polarization and topological phase transitions in monolayer ScX_2 (X = Cl, Br, I), Acta Mater. **246**, 118731 (2023).

[18] H. Huan, Y. Xue, B. Zhao, G. Gao, H. Bao, and Z. Yang, Strain-induced half-valley metals and topological phase transitions in MBr_2 monolayers (M = Ru, Os), Phys. Rev. B **104**, 165427 (2021).

[19] K. Sheng, B. Zhang, H.-K. Yuan, and Z.-Y. Wang, Strain-engineered topological phase transitions in ferrovalley 2H-$RuCl_2$ monolayer, Phys. Rev. B **105**, 195312 (2022).

[20] B. Huang, W.-Y. Liu, X.-C. Wu, S.-Z. Li, H. Li, Z. Yang, and W.-B. Zhang, Large spontaneous valley polarization and high magnetic transition temperature in stable two-dimensional ferrovalley YX_2 (X = I, Br, and Cl), Phys. Rev. B **107**, 045423 (2023).

[21] W. Xie, L. Zhang, Y. Yue, M. Li, and H. Wang, Giant valley polarization and perpendicular magnetocrystalline anisotropy energy in monolayer MX_2 (M = Ru, Os; X = Cl, Br), Phys. Rev. B **109**, 024406 (2024).

[22] G. Hussain, A. Fakhredine, R. Islam, R. M. Sattigeri, C. Autieri, and G. Cuono, Correlation-driven topological transition in Janus two-dimensional vanadates, Materials **16**, 1649 (2023).

[23] H. Hu, W.-Y. Tong, Y.-H. Shen, X. Wan, and C.-G. Duan, Concepts of the half-valley-metal and quantum anomalous valley Hall effect, npj Comput. Mater. **6**, 129 (2020).

[24] X. Feng, X. Xu, Z. He, R. Peng, Y. Dai, B. Huang, and Y. Ma, Valley-related multiple Hall effect in monolayer VSi_2P_4, Phys. Rev. B **104**, 075421 (2021).

[25] S.-D. Guo, Y.-L. Tao, W.-Q. Mu, and B.-G. Liu, Correlation-driven threefold topological phase transition in monolayer $OsBr_2$, Front. Phys. **18**, 33304 (2023).

[26] Y. C. Cheng, Z. Y. Zhu, M. Tahir, and U. Schwingenschlögl, Spin-orbit–induced spin splittings in polar transition metal dichalcogenide monolayers, Europhys. Lett. **102**, 57001 (2013).

[27] A.-Y. Lu *et al.*, Janus monolayers of transition metal dichalcogenides, Nat. Nanotechnol. **12**, 744 (2017).

[28] Y.-F. Zhao, Y.-H. Shen, H. Hu, W.-Y. Tong, and C.-G. Duan, Combined piezoelectricity and ferrovalley properties in Janus monolayer VClBr, Phys. Rev. B **103**, 115124 (2021).

[29] H. Sun, S.-S. Li, W. Ji, and C.-W. Zhang, Valley-dependent topological phase transition and quantum anomalous valley Hall effect in single-layer RuClBr, Phys. Rev. B **105**, 195112 (2022).

[30] Z. Liu, B. Zhou, X. Wang, and W. Mi, Two dimensional Janus RuXY (X, Y = Br, Cl, F, I, $X \neq Y$) monolayers: Ferromagnetic semiconductors with spontaneous valley polarization and tunable magnetic anisotropy, Phys. Chem. Chem. Phys. **25**, 25146 (2023).

[31] Y. Ma, Y. Wu, J. Tong, L. Deng, X. Yin, L. Zhou, X. Han, F. Tian, and X. Zhang, Distinct ferrovalley characteristics of the Janus RuClX (X = F, Br) monolayer, Nanoscale **15**, 8278 (2023).

[32] K. Jia, X.-J. Dong, S.-S. Li, W.-X. Ji, and C.-W. Zhang, First-principles study reveals an electronic correlation effect on the topological and electronic properties of Janus RuClF

monolayers: Implications for spintronics and valleytronics applications, ACS Appl. Nano Mater. **6**, 14003 (2023).
[33] G. Kresse and J. Hafner, *Ab initio* molecular dynamics for liquid metals, Phys. Rev. B **47**, 558 (1993).
[34] P. E. Blöchl, Projector augmented-wave method, Phys. Rev. B **50**, 17953 (1994).
[35] G. Kresse and J. Hafner, *Ab initio* molecular-dynamics simulation of the liquid-metal–amorphous-semiconductor transition in germanium, Phys. Rev. B **49**, 14251 (1994).
[36] G. Kresse and J. Furthmüller, Efficient iterative schemes for *ab initio* total-energy calculations using a plane-wave basis set, Phys. Rev. B **54**, 11169 (1996).
[37] A. Togo and I. Tanaka, First principles phonon calculations in materials science, Scr. Mater. **108**, 1 (2015).
[38] P. Asselin, R. F. L. Evans, J. Barker, R. W. Chantrell, R. Yanes, O. Chubykalo-Fesenko, D. Hinzke, and U. Nowak, Constrained Monte Carlo method and calculation of the temperature dependence of magnetic anisotropy, Phys. Rev. B **82**, 054415 (2010).
[39] V. Wang, N. Xu, J.-C. Liu, G. Tang, and W.-T. Geng, VASPKIT: A user-friendly interface facilitating high-throughput computing and analysis using VASP code, Comput. Phys. Commun. **267**, 108033 (2021).
[40] A. A. Mostofi, J. R. Yates, Y.-S. Lee, I. Souza, D. Vanderbilt, and N. Marzari, WANNIER90: A tool for obtaining maximally-localised Wannier functions, Comput. Phys. Commun. **178**, 685 (2008).
[41] Q. Wu, S. Zhang, H.-F. Song, M. Troyer, and A. A. Soluyanov, WannierTools: An open-source software package for novel topological materials, Comput. Phys. Commun. **224**, 405 (2018).
[42] See Supplemental Material at http://link.aps.org/supplemental/10.1103/PhysRevB.110.035128 for more details about the valley polarization with the in-plane magnetic moment, basis function in C_3 symmetry, coupling matrix elements between different d orbitals, MAE contribution in the first Brillouin zone, density of states, Wannier function fitting, strain-induced magnetic ground state, and magnetic anisotropy of H-RuClBr and OsClBr, respectively.
[43] A. T. Hoang *et al.*, Low-temperature growth of MoS_2 on polymer and thin glass substrates for flexible electronics, Nat. Nanotechnol. **18**, 1439 (2023).
[44] Y. Sun, Y. Zang, W. Tian, X. Yu, J. Qi, L. Chen, X. Liu, and H. Qiu, Plasma-induced large-area N,Pt-doping and phase engineering of MoS_2 nanosheets for alkaline hydrogen evolution, Energy Environ. Sci. **15**, 1201 (2022).
[45] Z. Liu *et al.*, General bottom-up colloidal synthesis of nano-monolayer transition-metal dichalcogenides with high 1T′-phase purity, J. Am. Chem. Soc. **144**, 4863 (2022).
[46] B. Huang *et al.*, Layer-dependent ferromagnetism in a van der Waals crystal down to the monolayer limit, Nature (London) **546**, 270 (2017).
[47] C. Gong *et al.*, Discovery of intrinsic ferromagnetism in two-dimensional van der Waals crystals, Nature (London) **546**, 265 (2017).
[48] P. Zhao, Y. Dai, H. Wang, B. Huang, and Y. Ma, Intrinsic valley polarization and anomalous valley Hall effect in single-layer 2H-$FeCl_2$, ChemPhysMater **1**, 56 (2022).
[49] R. Peng, Y. Ma, X. Xu, Z. He, B. Huang, and Y. Dai, Intrinsic anomalous valley Hall effect in single-layer Nb_3I_8, Phys. Rev. B **102**, 035412 (2020).
[50] X. Wang, R. Wu, D. Wang, and A. J. Freeman, Torque method for the theoretical determination of magnetocrystalline anisotropy, Phys. Rev. B **54**, 61 (1996).
[51] D. Dai, H. Xiang, and M.-H. Whangbo, Effects of spin-orbit coupling on magnetic properties of discrete and extended magnetic systems, J. Comput. Chem. **29**, 2187 (2008).
[52] M.-H. Whangbo, E. E. Gordon, H. Xiang, H.-J. Koo, and C. Lee, Prediction of spin orientations in terms of HOMO-LUMO interactions using spin-orbit coupling as perturbation, Acc. Chem. Res. **48**, 3080 (2015).
[53] Y. Wang, G. Yu, M. Rösner, M. I. Katsnelson, H.-Q. Lin, and S. Yuan, Polarization-dependent selection rules and optical spectrum atlas of twisted bilayer graphene quantum dots, Phys. Rev. X **12**, 021055 (2022).
[54] D. J. Thouless, M. Kohmoto, M. P. Nightingale, and M. den Nijs, Quantized Hall conductance in a two-dimensional periodic potential, Phys. Rev. Lett. **49**, 405 (1982).
[55] D. Xiao, M.-C. Chang, and Q. Niu, Berry phase effects on electronic properties, Rev. Mod. Phys. **82**, 1959 (2010).
[56] M. Ezawa, Photoinduced topological phase transition and a single Dirac-cone state in silicene, Phys. Rev. Lett. **110**, 026603 (2013).
[57] H. Rostami, R. Roldán, E. Cappelluti, R. Asgari, and F. Guinea, Theory of strain in single-layer transition metal dichalcogenides, Phys. Rev. B **92**, 195402 (2015).
[58] D. Wang, R. Wu, and A. J. Freeman, First-principles theory of surface magnetocrystalline anisotropy and the diatomic-pair model, Phys. Rev. B **47**, 14932 (1993).
[59] P. Bruno, Tight-binding approach to the orbital magnetic moment and magnetocrystalline anisotropy of transition-metal monolayers, Phys. Rev. B **39**, 865 (1989).